Reconstruction of Axisymmetric Temperature and Gas Concentration Distributions by Combining Fan-Beam TDLAS With Onion-Peeling Deconvolution

Reconstruction of Axisymmetric Temperature and Gas Concentration Distributions by Combining Fan-Beam TDLAS With Onion-Peeling Deconvolution

Chang Liu, Lijun Xu, *Senior Member, IEEE*, Zhang Cao, and Hugh McCann, *Senior Member, IEEE*

***Abstract*— Fan-beam tunable diode laser absorption spectroscopy (TDLAS) system was combined with onion-peeling deconvolution to reconstruct axisymmetric temperature and gas concentration distributions. The fan-beam TDLAS system consists of two tunable distributed feedback diode lasers at 7185.597 and 7444.36 cm^{-1}, a cylindrical lens and multiple photodiode detectors in a linear detector array. When a well-collimated laser beam penetrates through a cylindrical lens, a fan-beam laser was formed. Then, the fan-beam laser penetrates through the target region and is detected by the photodiode detectors in the detector array. After transforming the fan-beam geometry to equivalent parallel-beam geometry, axisymmetric temperature and gas concentration distributions can be reconstructed using the onion-peeling deconvolution. To obtain the reconstruction results with higher accuracy, a revised Tikhonov regularization method was adopted in the onion-peeling deconvolution. In this paper, numerical simulation and experimental verification were carried out to validate the feasibility of the proposed methods. The results show that the proposed methods can be used to on-line monitor the axisymmetric temperature and gas concentration distributions with higher accuracy and robustness in combustion diagnosis.**

***Index Terms*— Axisymmetric temperature and gas concentration distributions, fan-beam tunable diode laser absorption spectroscopy (TDLAS), onion-peeling deconvolution, regularization method.**

I. Introduction

TO MEET the standards on combustion efficiency and pollutant emissions nowadays, advanced temperature and gas concentration (simplified as concentration hereafter) measurement techniques are highly desired. In many practical combustion processes, the profiles of temperature and concentration are axisymmetrically distributed, or, to some extent, can be simplified as axisymmetrical. For instance, flat flame burners are used to generate stable, temperature-uniformed, and laminar flame, which are well known for their applications in flame calibration [1], [2], detailed investigations of flame stabilization processes [3], and heat transfer processes [4]. Influenced by the effects of heat transfer and convection between the core flow and the cold boundary of laboratory air, temperature, and concentration gradients from the center toward the outer parts of the flame are observable [5], which leads to cross section of the flame of the axisymmetric temperature and concentration distributions. Furthermore, rocket exhaust plume is another typical and significant example of combustion application with axisymmetric temperature and concentration distributions. As the exhaust gases expand beyond the nozzle exit, fuel rich species in the combustion gas reacts with the oxygen in the air, which contributes to afterburning reactions with axisymmetric temperature and concentration distributions in the plume backflow region [6]–[8]. Therefore, it is necessary to reconstruct the axisymmetric temperature and concentration distributions of the flame, to describe and monitor the combustion stability and flame characteristics of the combustion progress.

As a nonintrusive, fast, sensitive, and cost-effective optical absorption modality, tunable diode laser absorption spectroscopy (TDLAS) technique has gained widespread applications in accurate measurements of temperature and concentration of the combustion flow field. Generally, traditional line-of-sight TDLAS technique is employed to monitoring the average temperature and concentration of absorbing species in combustion field along the laser path [9]–[11]. Relying on measurements of multiple absorption transitions of a single species, the temperature probability density distribution along the laser path can be obtained [12], [13]. However, to some extent, these attempts are unable to obtain spatially resolved temperature and concentration distributions. For combustion of axisymmetric temperature and concentration distributions, Villarreal and Varghese [14] introduced a rapid tomographic inversion algorithm and set up a frequency-resolved absorption tomography system, to measure temperature and CO_2 concentration distributions in an atmospheric pressure flat flame

Manuscript received October 28, 2013; revised January 26, 2014; accepted March 10, 2014. Date of publication April 2, 2014; date of current version November 6, 2014. This work was supported in part by the National Science Foundation of China under Grant 61225006 and Grant 61327011, and in part by the Fundamental Research Funds for the Central Universities under Grant YWF-12-LTGF-198, Grant YWF-13-ZY-30, and Grant YWF-13-A01-054. The Associate Editor coordinating the review process was Dr. Wuqiang Yang. *(Corresponding author: L. Xu.)*

C. Liu, L. Xu, and Z. Cao are with the Key Laboratory of Precision Opto-Mechatronic Technology, Ministry of Education, The School of Instrument Science and Opto-Electronic Engineering, Beihang University, Beijing 100191, China (e-mail: lijunxu@buaa.edu.cn).

H. McCann is with the School of Engineering, University of Edinburgh, Edinburgh EH9 3JL, U.K.

Color versions of one or more of the figures in this paper are available online at http://ieeexplore.ieee.org.

Digital Object Identifier 10.1109/TIM.2014.2315737

burner. The burner was attached to a movable stage, so that it can move into or out of the optical path when the projection data are acquired. However, the structures of the TDLAS systems in the above attempts are rather complicated and difficult to realize on-line monitoring of the flame in real applications.

Compared with the parallel-beam laser, which each laser beam must be generated using a collimated lens, the fan-beam laser is much easier to generate using a well-collimated laser penetrates through a cylindrical lens [15]–[17]. Therefore, to simplify the optics structure and improve the imaging rate of the TDLAS system, the fan-beam laser was used instead of a parallel-beam laser. The axisymmetric temperature and gas concentration distributions can be solved by combining the TDLAS data with onion-peeling deconvolution. To increase the accuracy of the reconstructed distributions and make them less sensitive to noises, a revised Tikhonov regularization method, with its regularization parameter determined by L-curve curvature criterion, was adopted in the onion-peeling deconvolution.

II. Methodology

By calculating the integrated absorbance of the transitions, the TDLAS technique provides an accurate and fast way for measuring the temperature and concentration along the laser path. The onion-peeling deconvolution is widely used in tomographic reconstruction of axisymmetric objects by solving the Abel's equation [18]. Therefore, by combining TDLAS with the onion-peeling deconvolution, the axisymmetric temperature, and the concentration distributions can be reconstructed. However, the inherent ill-posedness of the Abel's equation leads to the reconstructed results more sensitive to noise. To treat this problem, the revised Tikhonov regularization method is adopted in the onion-peeling deconvolution, with its regularization parameter determined by L-curve curvature criterion.

A. Fundamentals of TDLAS

The principle of TDLAS technique had been previously described in [19]. When a well collimated laser at central wave number v [cm^{-1}] enters a gas sample with a total path length of L [cm], a proportion of light is absorbed and the fractional transmission is described as

$$\left(\frac{I_t}{I_0}\right)_v = \exp\left(-P\int_0^L X_{\mathrm{abs}}(x_l, y_l)S[T(x_l, y_l)]\phi_v dl\right) \quad (1)$$

where I_t and I_0 are the transmitted and incident laser intensities, respectively. P [atm] is the total pressure, $T(x_l,y_l)$ [K] the temperature at the local point (x_l,y_l), $X(x_l,y_l)$ the local mole fraction of the absorbing species, and φ_v [cm] the line-shape function. The line strength of transition $S[T(x_l,y_l)]$ [$\mathrm{cm}^{-2}\mathrm{atm}^{-1}$], is a function of the temperature as follows:

$$S(T) = S(T_0)\frac{Q(T_0)}{Q(T)}\left(\frac{T_0}{T}\right)\exp\left[-\frac{hcE''}{k}\left(\frac{1}{T}-\frac{1}{T_0}\right)\right] \times\left[1-\exp\left(\frac{-hcv_0}{kT}\right)\right]\left[1-\exp\left(\frac{-hcv_0}{kT_0}\right)\right]^{-1} \quad (2)$$

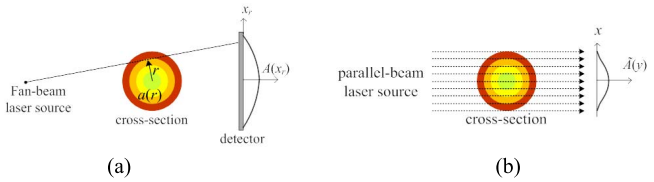

(a) (b)

Fig. 1. Illustration of (a) fan-beam geometry $A(x_r)$ and (b) equivalent parallel-beam geometry $\tilde{A}(x)$ transformed from the fan-beam geometry.

where h [J · s] is Planck's constant, c [cm · s^{-1}] the speed of light, k [J · K^{-1}] the Boltzmann's constant, $Q(T)$ the partition function of the absorbing molecule given by HITRAN [20], T_0 [K] the reference temperature (usually 296 K), v_0 [cm^{-1}] the line-center wave number, and E" [cm^{-1}] the lower energy of the transition.

The absorbance α_v is defined as

$$\alpha_v = -\ln\left(\frac{I_t}{I_0}\right)_v = \int_0^L X_{\mathrm{abs}}(x_l, y_l)S[T(x_l, y_l)]\phi_v dl. \quad (3)$$

Because the line-shape function φ_v is normalized so that $\int_{-\infty}^{\infty}\phi_v dv \equiv 1$, the integrated absorbance A [cm^{-1}] of the transition, which is defined as the area underneath the absorption line-shape function, can be inferred from (3) as

$$A = \int_{-\infty}^{\infty}\alpha_v dv = \int_0^L X_{\mathrm{abs}}(x_l, y_l)S[T(x_l, y_l)]dl = \int_0^L a(x_l, y_l)dl \quad (4)$$

where $a(x_l,y_l)$ denotes the local density of the integrated absorbance.

Under the assumption of the same pressure, mole fraction, and path length of the laser beam, the ratio of the simultaneously measured absorbance A of two transitions with different temperature dependence can be expressed as a function of the absorber temperature T only [21]

$$R = \frac{A_1}{A_2} = \frac{S_1(T)}{S_2(T)} = \frac{S_1(T_0)}{S_2(T_0)}\exp\left[-\frac{hc(E_1''-E_2'')}{k}\left(\frac{1}{T}-\frac{1}{T_0}\right)\right]. \quad (5)$$

Then, the average temperature along the laser path can be calculated as follows:

$$T = \frac{\frac{hc}{k}(E_2''-E_1'')}{\ln\frac{A_1}{A_2}+\ln\frac{S_2(T_0)}{S_1(T_0)}+\frac{hc}{k}\frac{(E_2''-E_1'')}{T_0}}. \quad (6)$$

It should be mentioned that (6) is commonly used for temperature measurements along the laser path through a region of uniform temperature distribution. Then, the average mole fraction can be obtained from the integrated absorbance A_1 and the known $S_1(T)$

$$X = \frac{A_1}{P\cdot S_1(T)\cdot L}. \quad (7)$$

B. Onion-Peeling Deconvolution

To simplify the structure and improve the imaging speed, the fan-beam geometry was used, as shown in Fig. 1(a). It should

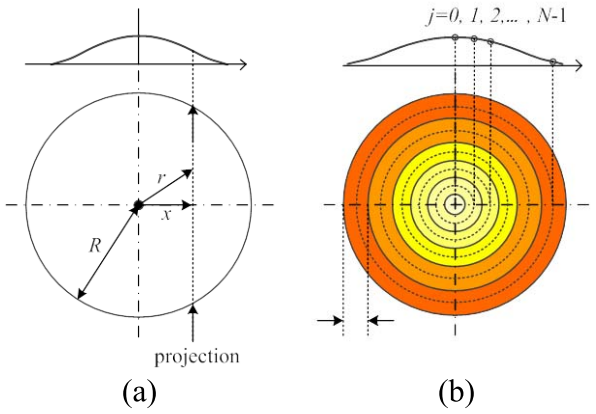

Fig. 2. (a) Geometry of the equivalent parallel-beam and (b) discretization of the flame domain.

be noted that the Abel's equation, which is used to reconstruct the axisymmetric object, is established in case of parallel-beam projection. Therefore, the fan-beam geometry should be transformed to the equivalent parallel-beam geometry with appropriate interpolation [22], [23], as shown in Fig. 1(b). As shown in [23], a two-step interpolation is implemented to transform the fan-beam geometry to the parallel-beam geometry. First, the fan-beam projections are interpolated into a set of fan-beam projections with a uniform distance to the central projection. Second, the uniform-distance fan-beam projections are interpolated to a set of uniformly spaced parallel-beam projections.

Under the assumption that the temperature and concentration on the cross section of the flame are axisymmetrically distributed, the radial densities of the integrated absorbances $a(r)$ are also axisymmetrically distributed according to (4). Consequently, the relationship between $\tilde{A}(x)$ and $a(r)$, is given by Abel's integral equation

$$\tilde{A}(x) = 2\int_y^R \frac{a(r)r}{\sqrt{r^2 - x^2}}dr \tag{8}$$

where x is the abscissa coordinate, r the radial coordinate of flame, and R the flame radius, as shown in Fig. 2(a).

An analytical solution of $a(r)$ can be obtained using the Abel transform as follows:

$$a(r) = -\frac{1}{\pi}\int_x^R \frac{\tilde{A}'(x)}{\sqrt{x^2 - r^2}}dx \tag{9}$$

where $\tilde{A}'(x) = \mathrm{d}\tilde{A}(x)/\mathrm{d}x$. However, in practical applications, (9) is of limited use because the analytical derivative of the projection data $\tilde{A}'(x)$. Usually, $\tilde{A}'(x)$ is unknown and approximated by a finite-difference scheme, which is sensitive to the error in the projection data $\tilde{A}(x)$. Therefore, by transforming the Abel's integral equation from the continuous domain into the discrete domain, the onion-peeling deconvolution is introduced. First, the flame is discretized into N annular elements. The width Δr equals to $R/(N–1/2)$. As shown in Fig. 2(b), the solution $a(r)$ can be assumed to a constant within each element. Then, (8) can be discretized into

$$\tilde{A} = 2\sum_{j=i}^{N-1} a_j \int_{\substack{r_j,j=i \\ r_j-\Delta r/2, j>i}}^{r_j+\Delta r/2} \frac{r}{\sqrt{r^2 - y_i^2}}dr \tag{10}$$

where $y_i = i\,\Delta r$, $r_j = j\,\Delta r$, $\tilde{A}_i = \tilde{A}(y_i)$, and a_j approximates $a(r_j)$. In general, (10) can be simplified as

$$\mathbf{D}_{\mathrm{OP}}\boldsymbol{a} = \tilde{\mathbf{A}} \tag{11}$$

where $\boldsymbol{a}^{\mathrm{T}} = \{a_0, a_1, \ldots, a_{N-1}\}$, $\tilde{A}^{\mathrm{T}} = \{\tilde{A}_0, \tilde{A}_1, \ldots, \tilde{A}_{N-1}\}$, and $\mathbf{D}_{\mathrm{OP}}$ the upper triangular matrix in the onion-peeling deconvolution

$$\mathbf{D}_{\mathrm{OP},ij} = \begin{cases} 0, & j < i \\ 2\Delta r\left[(j+1/2)^2 - i^2\right]^{1/2}, & j = i \\ 2\Delta r\left\{\left[(j+1/2)^2 - i^2\right]^{1/2} - \left[(j-1/2)^2 - i^2\right]^{1/2}\right\}, & j > i. \end{cases} \tag{12}$$

The element $\mathbf{D}_{\mathrm{OP},ij}$ denotes the contribution of $\boldsymbol{a}(r_j)$ to the projection data $\tilde{A}(x_i)$. Using back substitution, the vector $\boldsymbol{a}$ can be solved as follows:

$$\boldsymbol{a} = \mathbf{D}_{\mathrm{OP}}^{-1}\tilde{\mathbf{A}}. \tag{13}$$

According to (6), if the radial densities of the integrated absorbance $a_1(r_j)$ and $a_2(r_j)$ of two transitions are retrieved, the radial temperature $T(r_j)$ can be calculated by

$$T(r_j) = \frac{\frac{hc}{k}(E_2'' - E_1'')}{\ln\frac{a_1(r_j)}{a_2(r_j)} + \ln\frac{S_2(T_0)}{S_1(T_0)} + \frac{hc}{k}\frac{(E_2'' - E_1'')}{T_0}}. \tag{14}$$

With the reconstructed radial temperature $T(r_j)$ in hand, the radial concentration (mole fraction) $X(r_j)$ can be determined by

$$X(r_j) = \frac{a_1(r_j)}{S_1[T(r_j)]}. \tag{15}$$

C. Revised Tikhonov Regularization Method

It is known that the Abel's integral equation is a first kind Volterra integral equation, which is inherent ill-posed and sensitive to noise-contaminated projection data [24]. To treat this problem, regularization methods are good candidates. Using the properties of both TSVD and Tikhonov regularization methods [25], [26], a revised Tikhonov regularization method is proposed.

Using singular value decomposition, the matrix $\mathbf{D}_{\mathrm{OP}}$ in (11) is factorized into

$$\mathbf{D}_{\mathrm{OP}} = \mathbf{U}\sum\mathbf{V}^T \tag{16}$$

where $\mathbf{U} = \{u_0, u_1, \ldots, u_{N-1}\}$ and $\mathbf{V} = \{v_0, v_1, \ldots, v_{N-1}\}$ are two orthogonal matrixes, Σ is the diagonal matrix with singular values σ_j

$$\sum = \mathrm{diag}[\sigma_0, \sigma_1, \ldots, \sigma_{N-1}]. \tag{17}$$

Here, $\{\sigma_j | j = 0, 1, \ldots, N–1\}$ satisfy $\sigma_j > 0$ and are ordered as $\sigma_0 \geq \sigma_1 \geq \cdots \geq \sigma_{N-1}$. All the singular values decay gradually to zero, and the condition number of

$\mathbf{D}_{\mathrm{OP}}$, $\mathrm{cond}(\mathbf{D}_{\mathrm{OP}}) = \sigma_0/\sigma_{N-1}$, becomes larger as N increases. Actually, the smaller singular values contribute more to the error of the solution than the larger singular values. Therefore, the smaller singular values need to be dampened by using the revised Tikhonov regularization method.

When σ_j is larger than the regularization parameter λ, i.e., $\sigma_j < \lambda$, we do not damp σ_j. When $\sigma_j \leq \lambda$, we damp σ_j with $\sigma_j^2 + \lambda^2$. Suppose that $\sigma_k < \lambda \geq \sigma_{k+1}$, the solution vector of $\boldsymbol{a}$ is given by

$$\boldsymbol{a} = \sum_{j=0}^{k} \frac{u_j^T \tilde{\mathbf{A}}}{\sigma_j} v_j + \sum_{j=k+1}^{N-1} \frac{\sigma_j}{\sigma_j^2 + \lambda^2} u_j^T \tilde{\mathbf{A}} v_j \tag{18}$$

or

$$\boldsymbol{a} = \mathbf{V}\mathbf{D}_\lambda \sum^{T} \mathbf{U}^T \tilde{\mathbf{A}} v_j \tag{19}$$

where $\mathbf{D}_\lambda = \mathrm{diag}[\sigma_0^2, \sigma_1^2, \ldots, \sigma_k^2, (\sigma_{k+1}^2 + \lambda^2), \ldots, (\sigma_{N-1}^2 + \lambda^2)]$. Furthermore, the criteria for choosing $\lambda$is to obtain a balance between losing information and acquiring a stable solution. Here, the L-curve curvature criterion is adopted to obtain appropriate λ [27].

III. Results and Discussion

A. Numerical Simulations

1) Simulation Condition: Water vapor (H_2O), which is a major product among combustion exhaust, has several thousand absorption transitions in near-infrared. Compared with other species, it is much easier to choose absorption transitions of water vapor with appropriate line strengths and good temperature sensitivities. Therefore, H_2O was selected as the target absorbing species in the simulation and experiment. According to the criteria of line selection discussed in [10] and [28], two main criteria were used to select two transitions in this paper. First, the absorption strength should be moderate. Too large absorption strength will lead to a too small signal in the detector, whereas too small absorption strength will not be differentiated by the detector. Second, according to the flame characteristics discussed in Section II, suitable lower state energy E" should be provided to ensure high sensitivity in the temperature range. To satisfy the above criteria, the H_2O transitions of 7185.597 and 7444.36 cm^{-1}, which can be accessed by the distributed feedback (DFB) laser diodes available in our laboratory, were used both in simulation and experiment, as shown in Table I. It should be noted that although the selected transitions may not be the optimum choices, good temperature sensitivity can be acquired for the given temperature range, as shown in Fig. 3.

Furthermore, both in the simulation and experiment, the pressure can be assumed to be uniform and known, that is 1 atm, when the flame is burnt in the room air. The radius of circular target region was 3 cm. The distance between the fan-beam laser source and the center of the flame was 20 cm. The fan-beam laser covers the flame with 18° and was detected by 15 equally spaced photodiode detectors, which were used to obtain 15 integrated absorbances, i.e., 15 projection data. Under the assumption that the flame is axisymmetric, half of the projection data are redundant, since the left and right detectors from the center of the fan-beam laser display mirrored values. In part B of this Section, the redundant projection data are used to justify the axisymmetric assumption of the flame. For the right eight projection data from the central projection data, a total number of 40 interpolated projection data were obtained using spline interpolation. According to (11), the number of the discretized annular elements of the flame, N, equals to the number of the projection data, i.e., $N = 40$, that is, the width of the discretized annular element, Δr, approximately equals to 0.075 cm.

TABLE I
Two H_2O Absorption Transitions Selected for Simulation and Experiment

Line index	Wave Number v_0 [cm^{-1}]	S at 296 K [$\mathrm{cm}^{-2}\mathrm{atm}^{-1}$]	E" [cm^{-1}]
1	7185.597	1.96×10^{-2}	1045.058
2	7444.36	1.10×10^{-3}	1786.00

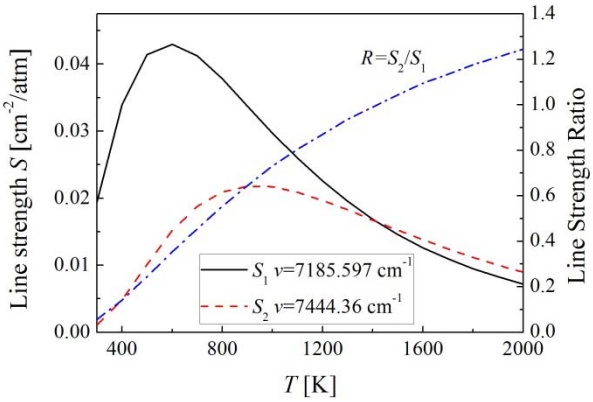

Fig. 3. Dependence of line strength of transitions on temperature. The temperature sensitivity is inferred from the line strength ratio of two transitions.

2) Flame Characterization: A circular flame burner was used to generate a flame with axisymmetric temperature and concentration distributions. The methane and dry air were well premixed and transferred to the chamber at the bottom of the burner. The mixed fuel gas were then released to air through a porous stainless steel distributer with a diameter of 50 mm, as shown in Fig. 4(a). Majority of the holes were distributed axisymmetrically around the boundary and the other holes were distributed axisymmetrically in the central area of the distributer. After striking sparks near the distributer, a relatively stable laminar flame was generated above the distributer in a windless laboratory. Due to axisymmetrically distributed holes on the porous stainless steel distributer, a flame with axisymmetric temperature, and H_2O concentration distributions was generated. Furthermore, influenced by the larger porosity around the boundary, a higher flow rate of the fuel was introduced, which consequently resulted in a greater heat release and a higher temperature around the boundary than that around the central area. The photo of the

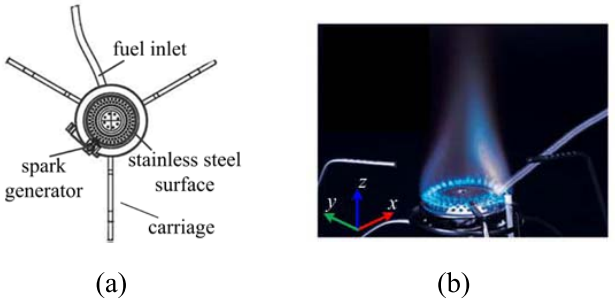

Fig. 4. (a) Schematic of the circular flame burner. (b) Photo of the flame with nonuniform temperature profile generated by the burner.

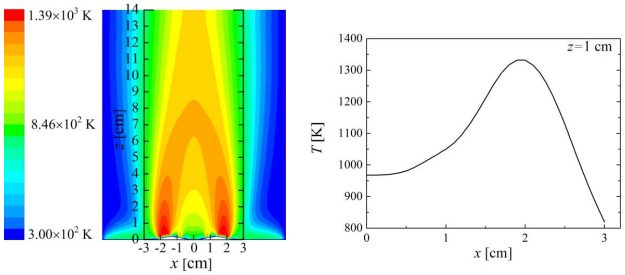

Fig. 5. (a) Temperature contours in the computation domain. (b) Temperature distributions along x-axis at the height of $z = 1$ cm.

flame shown in Fig. 4(b) clearly shows that the boundary of the flame is brighter than its center.

To obtain a reasonable overview on the temperature and H_2O concentration distributions generated by the burner, numerical calculation of the mole fraction of water vapor was carried out through computational fluid dynamic simulation. The simulation was implemented by utilizing the finite element analysis software package ANSYS FLUENT.

In the simulation, a 2-D computation domain was established, which is the same as a vertical-section along z-axis of the burner. Methane and air were well premixed at room temperature with an equivalence ratio of 0.6. The premixed fuel were released through the distributer with a velocity magnitude of 10 mm/s and burnt sufficiently in the air. After the iterative calculation was converged, we obtained the temperature and H_2O concentration distributions of the computation domain, as shown in Figs. 5(a)and 6(a), respectively. It can be seen that the nonuniformity of temperature distribution along x-axis is more significant than that of the concentration distribution. It can also be observed from Fig. 5(a) that the nonuniformity of temperature distribution along x-axis at a larger height is more significant than that at a smaller height. To examine the performance of the proposed methods for a larger temperature range and temperature gradient along x-axis, distributions of the temperature and H_2O concentration along the x-axis on the height of 1 cm above the burner were extracted, as shown in Figs. 5(b) and 6(b), respectively. Furthermore, the flame is more stable near the porous stainless steel distributer of the burner, where the well-premixed fuel is released. Influenced by the effects of convection between the core flow and the laboratory air, the flame at a larger height fluctuates more severely than that at a smaller height

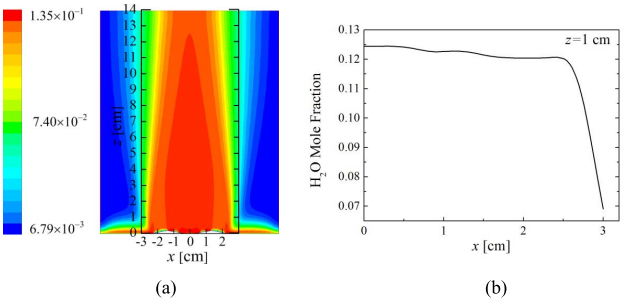

Fig. 6. (a) H_2O concentration (mole fraction) contours of water vapor in the computation domain. (b) H_2O concentration values along x-axis at the height of $z = 1$ cm.

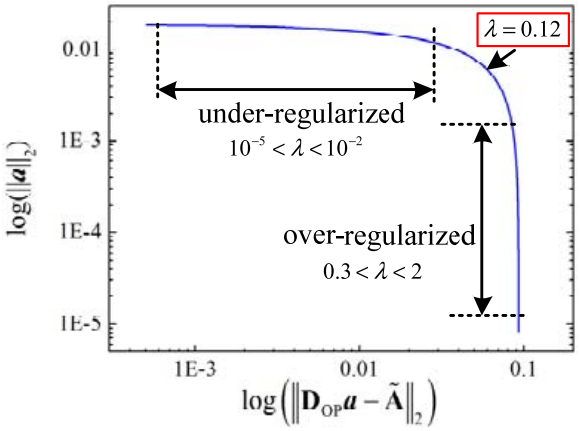

Fig. 7. Generic form of the L-curve for $N = 40$.

3) Numerical Results and Discussions: As discussed in part C of Section II, the regularization parameter λ is determined using the L-curve curvature criterion. For $N = 40$, the norms of the solution $\log(\|\boldsymbol{a}\|_2)$ and the norms of residual vectors $\log(\|\mathbf{D}_{\mathrm{OP}}\boldsymbol{a} - \tilde{\mathbf{A}}\|_2)$ obtained using different λ were plotted. As shown in Fig. 7, when λ ranges from 10^{-5} to 10^{-2}, the solution of (11) is under-regularized, indicating that (11) is correctly solved but the solution is highly sensitive to the noise-contaminated $\tilde{\mathbf{A}}$. When λ ranges from 0.5 to 2, the solution is overregularized, indicating that the solution of (11) is smooth but not accurate enough. When λ equals 0.32, the point on the L-curve corresponds to the maximum curvature of the curve, indicating that a balance between the accuracy and the smoothness of the solution is acquired. Consequently, the regularization parameter λ is selected as 0.32.

In practical measurements, the data acquired by the detector are always contaminated with random noise, which may come from the circuits, the tiny fluctuation of laser power, and so on. Furthermore, gas refractive index for near infrared light is dependent on temperature gradient of the flame, which may cause laser beam steering. However, according to [29] and [30], the relative change of the gas refractive index is calculated for the flame in this paper, and proved to be smaller than 0.005%, which can be neglected compared with the random noises from the circuits and the tiny fluctuation of laser power. Therefore, to examine the performance of the proposed methods for noise-contaminated data, additional random noise is imposed on the integrated absorbances. In general, the level

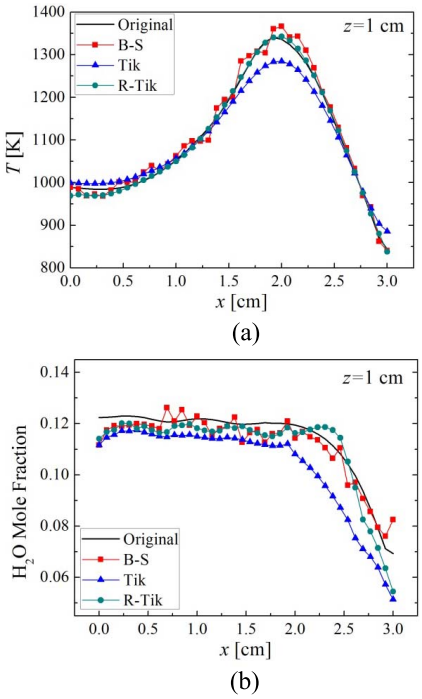

Fig. 8. (a) Temperature and (b) H_2O concentration along x-axis at the height of $z = 1$ cm, reconstructed in the simulation by the onion-peeling deconvolution when adopting the back substitution (B-S), Tikhonov regularization method (Tik), and the revised Tikhonov regularization method (R-Tik), respectively.

of noise is described by signal-to-noise ratio (SNR), which is calculated by

$$\mathrm{SNR} = 20\log(S/N) \tag{20}$$

where S and N denote the noise-free data and the noise in the measured data, respectively.

By adding 1% random noise on the projection data, that is, the SNR equals to 40 dB, $T(r_j)$ and $X(r_j)$ were reconstructed using the onion-peeling deconvolution when adopting the back substitution, the Tikhonov regularization method, and the revised Tikhonov regularization method, respectively. As shown in Fig. 8, the smoothness of the $T(r_j)$ and $X(r_j)$ reconstructed using the regularization methods are better than those obtained using the back substitution. Furthermore, $T(r_j)$ and $X(r_j)$ obtained by the revised Tikhonov regularization method better fit the original ones than those obtained using Tikhonov regularization method, indicating that $T(r_j)$ and $X(r_j)$ retrieved using the proposed method are more accurate.

B. Experiments and Results

1) Experimental System: As shown in Fig. 9, the experimental system consists of two DFB diode lasers (NLK1E5EAAA, NEL) with line-width of 10 MHz and output power of 10 mW, each controlled independently by a laser diode controller (LDC 3900, ILX Lightwave). The laser diode controller provides temperature and current control for the DFB lasers. The current of both controllers was simultaneously modulated by a ramp signal from a double-channel function generator (AFG3102, Tektronix), so that the wavelengths of the DFB lasers can be scanned within a spectral range of $\sim$1.5 cm^{-1} around the central wavelengths. It should be noted that the two absorption signals were obtained using a time division multiplexing scheme [10], [31]. In detail, each laser was scanned at a rate of 5 kHz. During a scanning period, the current was set under the lower working threshold of the DFB laser for 0.25 ms and was scanned by the ramp signal for 0.15 ms. The phase difference of the double-channel scanning signals was 180°. By combining the two lasers with a single mode 2×2 fiber-couplers, the absorption signals for the two transitions in Table I can be obtained within 0.4 ms, as shown in Fig. 10. To yield a background signal and correct the combustion emission, a further 0.1 ms is required to set the current underneath the lower working limit of the threshold.

Subsequently, the 2×2 fiber-coupler splits the laser into two channels. The laser in the first channel is collimated and delivered into a solid etalon with a free spectral range of 2.53 GHz (0.084 cm^{-1}) to monitor the wave number during the wavelength scanning. Since the peak-to-peak separation in the FSR signals is constant (equaling to the FSR), the transformation from the time to the relative wave number can be easily obtained. The laser in the second channel is collimated and transmitted through a cylindrical lens (focal length f equals 4.0 mm) to form a fan-beam laser. The fan-beam laser then penetrates the target flame and is detected by 15 equally spaced photodiode detectors. The optical signals are transferred by the photodiode detectors to current signals. In conjunction with a current-to-voltage converter, most often a transimpedance amplifier [32], the voltage signals are sampled by a data acquisition instrument into a computer to calculate the integrated absorbances of the projections. The optics, detectors, and the open paths are purged with nitrogen, to eliminate the interference absorption by H_2O vapor in room air.

2) Experimental Results and Discussions: The integrated absorbances of the absorption signals in Fig. 10 were obtained using the following steps. First, the nonabsorbing wings of the absorption signals were extracted and used to fit the baseline. Second, by subtracting the absorption signals from the fitted baselines, the absorption spectra were calculated. Third, multipeak Voigt profiles were used to fit the absorption spectra and the interference neighboring peaks obtained in the second step, as shown in Fig. 11. Finally, the integrated absorbances were calculated based on the Voigt fit of the central wavelengths, i.e., 7185.597 and 7444.36 cm^{-1}, which are obtained in the third step.

As discussed in the part A of this Section, if the flame is axisymmetric, the left and right photodiode detectors from the center of the fan-beam laser should display mirrored projection data. Therefore, half of the projection data are redundant and are used to justify the axisymmetric assumption of the flame. By continuously scanning two transitions for 100 times, the distributions of the integrated absorbances of two transitions, A_1 and A_2, were obtained by calculating the mean of 100 integrated absorbances. As shown in Fig. 12, the mean values of A_1 and A_2 are symmetrically distributed, indicating that the temperature and concentration distributions of the flame can be assumed to be axisymmetric. The largest integrated absorbances occur in the center, while those

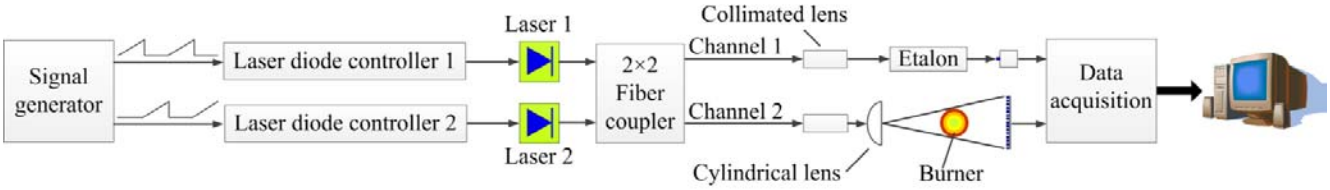

Fig. 9. Schematic of the fan-beam TDLAS system.

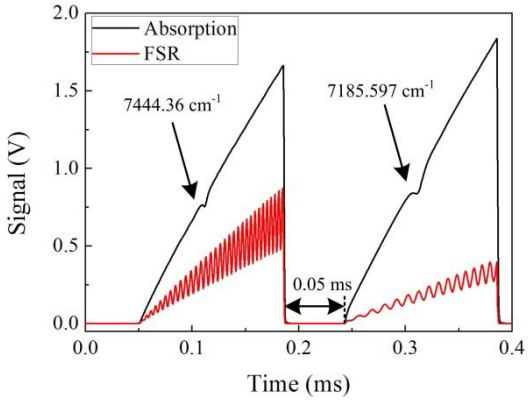

Fig. 10. Absorption and FSR signals obtained by the TDM scheme.

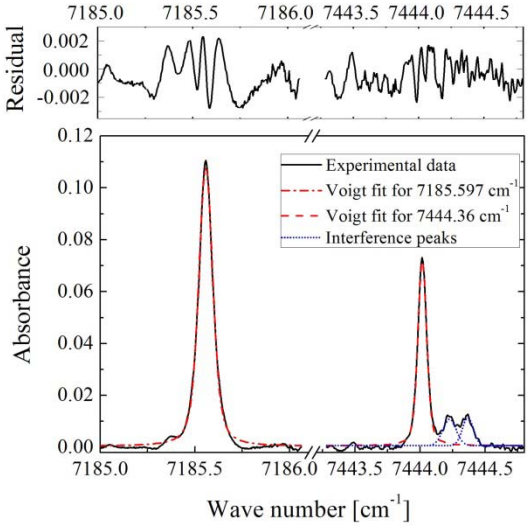

Fig. 11. Multipeak Voigt fitting and the residual of the transitions at 7185.597 and 7444.36 cm^{-1}, respectively.

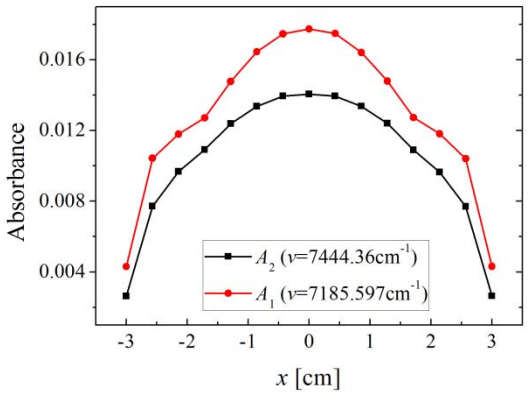

Fig. 12. Distributions of the integrated absorbances of the transitions at 7185.597 cm^{-1} (A_1) and 7444.36 cm^{-1}(A_2), along x-axis, respectively.

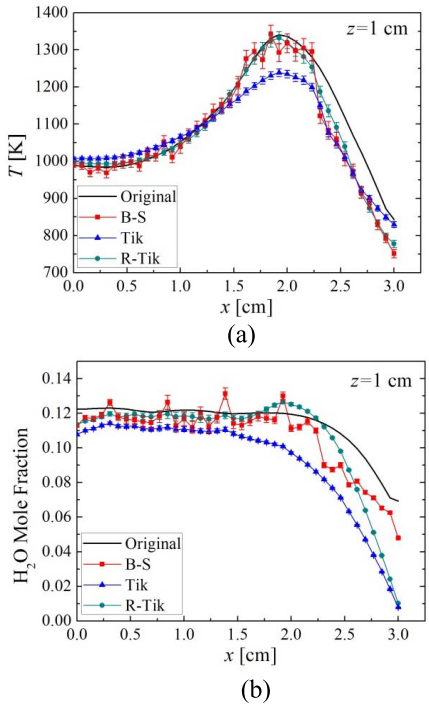

Fig. 13. (a) Mean values with their standard deviations of temperature and (b) H_2O concentration, along x-axis at the height of $z = 1$ cm, reconstructed in the experiment by the onion-peeling deconvolution when adopting the back substitution (B-S), Tikhonov regularization method (Tik), and the revised Tikhonov regularization method (R-Tik), respectively.

gradually decrease from the center to the boundary of the area covered by the fan beam.

The circular flame burner was fixed on an adjustable platform. By adjusting the vertically distance of the platform, the flame at the height of $z = 1$ cm is projected by the fan-beam laser. Then, the radial temperature and H_2O concentration at $z = 1$ cm are reconstructed by the onion-peeling deconvolution, and the revised Tikhonov regularization method is adopted in the onion-peeling deconvolution. To examine the effectiveness of the proposed methods, the reconstructed temperature and H_2O concentration distributions with their standard deviations for the 100 measurements are shown in Fig. 13. The midpoint signifies the mean of the 100 solutions of $T(r_j)$ and $X(r_j)$, and the error bar to each midpoint denotes the standard deviation of the 100 solutions. It can be seen that the standard deviation of $T(r_j)$ and $X(r_j)$ obtained using the Tikhonov and the revised Tikhonov regularization methods are smaller than those obtained using the back substitution method, denoting that the regularization methods are more robust and necessary to be adopted in the onion-peeling

deconvolution. Particularly, the mean values of $T(r_j)$ and $X(r_j)$ retrieved by the revised Tikhonov regularization method are also more smooth and accurate than the other methods.

Compared with the reconstructed results in Fig. 8, the errors between the reconstructed $T(r_j)$ and $X(r_j)$ are larger at the boundary than those in the central areas, which is mainly caused by the disturbance of air at the boundary of the flame. It should also be noted that the water vapor transitions chosen in this paper is not completely optimal for the whole temperature range. It is more sensitive for the temperature from $\sim$500 to $\sim$1200 K, but not for temperature higher than 1200 K. Therefore, large temperature variations appear at higher temperature in Fig. 13(a).

IV. Conclusion

In this paper, the axisymmetric temperature and gas concentration distributions were reconstructed by combining fan-beam TDLAS with the onion-peeling deconvolution. To improve the accuracy of the reconstruction results, the revised Tikhonov regularization method is adopted in the onion-peeling deconvolution, with its regularization parameter determined by L-curve curvature criterion.

For the axisymmetric temperature and H_2O concentration distributions generated by the circular flame burner, numerical simulations were carried out using the projection data with 1% random noises. After transforming the fan-beam geometry to equivalent parallel-beam geometry, the axisymmetric temperature, and H_2O concentration distributions were reconstructed using the onion-peeling deconvolution and the revised Tikhonov regularization method. The results obtained by the proposed method better fit the original ones than those obtained using the back substitution and Tikhonov regularization method. In the experiment, the errors between the reconstructed results and the simulated ones are larger at the boundary than those in the central areas, which are mainly caused by the disturbance of environmental air at the boundary of the flame.

References

[1] M. A. Gregor and A. Dreizler, "A quasi-adiabatic laminar flat flame burner for high temperature calibration," *Meas. Sci. Technol.*, vol. 20, no. 6, pp. 065402-1–065402-7, 2009.

[2] G. Hartung, J. Hult, and C. F. Kaminski, "A flat flame burner for the calibration of laser thermometry techniques," *Meas. Sci. Technol.*, vol. 17, no. 9, pp. 2485–2493, 2006.

[3] L. P. H. de Goey, A. van Maaren, and R. M. Quax, "Stabilization of adiabatic premixed laminar flames on a flat flame burner," *Combustion Sci. Technol.*, vol. 92, nos. 1–3, pp. 201–207, 1993.

[4] K. J. Bosschaart and L. P. H. de Goey, "Detailed analysis of the heat flux method for measuring burning velocities," *Combustion Flame*, vol. 132, no. 1, pp. 170–180, 2003.

[5] F. Migliorini, S. De Iuliis, F. Cignoli, and G. Zizak, "How 'flat' is the rich premixed flame produced by your McKenna burner?" *Combustion Flame*, vol. 153, no. 3, pp. 384–393, 2008.

[6] W. Wang, Z. Wei, Q. Zhang, N. Wang, and Y. Xiong, "Infrared radiation signature of exhaust plume from solid propellants of different energy characteristics," in *Proc. 47th AIAA/ASME/SAE/ASEE Joint Propuls. Conf. Exhibit*, 2011.

[7] J. M. Burt and I. D. Boyd, "High altitude plume simulations for a solid propellant rocket," *AIAA J.*, vol. 45, no. 12, pp. 2872–2884, 2007.

[8] F. Zhang, T. Fujiwara, and K. Komurasaki, "Diode-laser tomography for arcjet plume reconstruction," *Appl. Opt.*, vol. 40, no. 6, pp. 957–964, 2001.

[9] X. Chao, J. Jeffries, and R. Hanson, "Real-time, in situ, continuous monitoring of CO in a pulverized-coal-fired power plant with a 2.3 μm laser absorption sensor," *Appl. Phys. B*, vol. 110, no. 3, pp. 359–365, 2013.

[10] F. Li *et al.*, "Simultaneous measurements of multiple flow parameters for scramjet characterization using tunable diode-laser sensors," *Appl. Opt.*, vol. 50, no. 36, pp. 6697–6707, 2011.

[11] J. T. C. Liu *et al.*, "Near-infrared diode laser absorption diagnostic for temperature and water vapor in a scramjet combustor," *Appl. Opt.*, vol. 44, no. 31, pp. 6701–6711, 2005.

[12] X. Liu, J. B. Jeffries, and R. K. Hanson, "Measurement of non-uniform temperature distributions using line-of-sight absorption spectroscopy," *AIAA J.*, vol. 45, no. 2, pp. 411–419, 2007.

[13] S. T. Sanders, J. Wang, J. B. Jeffries, and R. K. Hanson, "Diode-laser absorption sensor for line-of-sight gas temperature distributions," *Appl. Opt.*, vol. 40, no. 24, pp. 4404–4415, 2001.

[14] R. Villarreal and P. Varghese, "Frequency-resolved absorption tomography with tunable diode lasers," *Appl. Opt.*, vol. 44, no. 31, pp. 6786–6795, 2005.

[15] P. Wright *et al.*, "Toward in-cylinder absorption tomography in a production engine," *Appl. Opt.*, vol. 44, no. 31, pp. 6578–6592, 2005.

[16] E. J. Beiting, "Fiber-optic fan-beam absorption tomography," *Appl. Opt.*, vol. 31, no. 9, pp. 1328–1343, 1992.

[17] E. J. Beiting, "Fast optical absorption tomography," *Opt. Lett.*, vol. 16, no. 16, pp. 1280–1282, 1991.

[18] C. J. Dasch, "One-dimensional tomography: A comparison of Abel, onion-peeling, and filtered backprojection methods," *Appl. Opt.*, vol. 31, no. 8, pp. 1146–1152, 1992.

[19] M. G. Allen, "Diode laser absorption sensors for gas-dynamic and combustion flows," *Meas. Sci. Technol.*, vol. 9, no. 4, pp. 545–562, 1998.

[20] L. S. Rothman *et al.*, "The HITRAN 2008 molecular spectroscopic database," *J. Quant. Spectrosc. Radiat. Transf.*, vol. 110, no. 9, pp. 533–572, 2009.

[21] X. Liu, J. B. Jeffries, R. K. Hanson, K. M. Hinckley, and M. A. Woodmansee, "Development of a tunable diode laser sensor for measurements of gas turbine exhaust temperature," *Appl. Phys. B, Lasers Opt.*, vol. 82, no. 3, pp. 469–478, 2006.

[22] L. Xu, Y. Han, L. Xu, and J. Yang, "Application of ultrasonic tomography to monitoring gas/liquid flow," *Chem. Eng. Sci.*, vol. 52, no. 13, pp. 2171–2183, 1997.

[23] J. Hsieh, *Computed Tomography: Principles, Design, Artifacts, and Recent Advances*. Bellingham, WA, USA: SPIE, 2009.

[24] R. Gorenflo and S. Vessella, *Abel Integral Equations: Analysis and Applications*. Berlin, Germany: Springer-Verlag, 1993.

[25] A. N. Tikhonov and V. Y. Arsenin, *Solutions of Ill-Posed Problems*. Washington, DC, USA: Winston, 1977.

[26] C. Liu, L. Xu, and Z. Cao, "Measurement of nonuniform temperature and concentration distributions by combining line-of-sight tunable diode laser absorption spectroscopy with regularization methods," *Appl. Opt.*, vol. 52, no. 20, pp. 4827–4842, 2013.

[27] P. C. Hansen and D. P. O'Leary, "The use of the L-curve in the regularization of discrete ill-posed problems," *SIAM J. Sci. Comput.*, vol. 14, no. 6, pp. 1487–1503, 1993.

[28] X. Zhou, J. B. Jeffries, and R. K. Hanson, "Development of a fast temperature sensor for combustion gases using a single tunable diode laser," *Appl. Phys. B, Lasers Opt.*, vol. 81, no. 5, pp. 711–722, 2005.

[29] R. J. Hill, S. F. Clifford, and R. S. Lawrence, "Refractive-index and absorption fluctuations in the infrared caused by temperature, humidity, and pressure fluctuations," *J. Opt. Soc. Amer. A*, vol. 70, no. 10, pp. 1192–1205, 1980.

[30] J. C. Owens, "Optical refractive index of air: Dependence on pressure, temperature and composition," *Appl. Opt.*, vol. 6, no. 1, pp. 51–59, 1967.

[31] S. Karagiannopoulos, E. Cheadle, P. Wright, S. Tsekenis, and H. McCann, "Multiwavelength diode-laser absorption spectroscopy using external intensity modulation by semiconductor optical amplifiers," *Appl. Opt.*, vol. 51, no. 34, pp. 8057–8067, 2012.

[32] P. Wright, K. B. Ozanyan, S. J. Carey, and H. McCann, "Design of high-performance photodiode receivers for optical tomography," *IEEE Sensors J.*, vol. 5, no. 2, pp. 281–288, Apr. 2005.

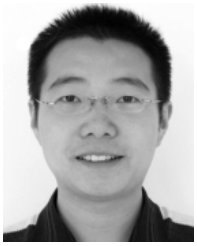

Chang Liu received the B.Sc. degree in automation from the School of Electrical Engineering and Automation, Tianjin University, Tianjin, China, in 2010. He is currently pursuing the Ph.D. degree in measurement technologies and instruments from the School of Instrument Science and Opto-Electronic Engineering, Beihang University, Beijing, China.

His current research interests include tunable diode laser absorption spectroscopy (TDLAS), laser absorption tomography, temperature and gas concentration measurement, and TDLAS system hardware design.

Zhang Cao received the B.Sc. (Hons.) degree in automation and the M.Eng. and Ph.D. (Hons.) degrees in measurement technology and automatic devices from Tianjin University, Tianjin, China, in 2003, 2005, and 2008, respectively.

He is currently an Associate Professor with the School of Instrument Science and Opto-Electronic Engineering, Beihang University, Beijing, China. His current research interests include process tomography, multiphase flow measurement, inverse problems, and particle sizing.

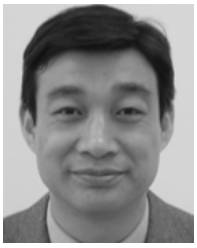

Lijun Xu (M'04–SM'04) received the B.Sc., M.Eng., and Ph.D. degrees in electrical engineering and instrumentation from Tianjin University, Tianjin, China, in 1990, 1993, and 1996, respectively.

He was an Associate Professor with the School of Electrical Engineering and Automation, Tianjin University, from 1997 to 2001, a Research Fellow with the University of Greenwich at Medway, London, U.K., and the University of Kent, Canterbury, U.K., from 2002 to 2004. He was a Higher Scientific Officer with the Department of Physics, Institute of Cancer Research, University of London, London, from 2004 to 2006. He is currently a Professor with the School of Instrument Science and Opto-Electronic Engineering, Beihang University, Beijing, China. He has authored and co-authored more than 200 publications. His current research interests include digital imaging and dynamic process monitoring.

Dr. Xu is a recipient of the National Science Fund for Distinguished Young Scholars of China, the Ministry of Education Technology Invention Award, the Tianjin Natural Science Award, and the Sixth Tianjin Youth Science and Technology Award. He was nominated as a key teacher in higher education and an excellent researcher in the new century by the Ministry of Education, China, in 2000 and 2007, respectively.

Hugh McCann (SM'03) received the B.Sc. and Ph.D. degrees from the University of Glasgow, Glasgow, U.K., in 1976 and 1980, respectively.

He was a Professor of Tomographic Imaging and the Head of the School of Engineering at the University of Edinburgh, Edinburgh, U.K., in 2013. From 1996 to 2013, he was a Professor of Industrial Tomography with the University of Manchester, Manchester, U.K., following 10 years in research and development with the Royal Dutch/Shell Group. He was involved in high-energy particle physics for 10 years at Glasgow, Manchester, CERN, Geneva, Switzerland, and DESY, Hamburg, Germany. He has extended industrial tomography to provide specific chemical contrast using high-speed all-optoelectronic techniques, and has developed electrical impedance tomography for medical applications, collaborating intensively with users in both academia and industry. He was the Head of the School of Electrical and Electronic Engineering, Manchester, from 1999 to 2002, the Chair of the U.K. Professors and the Head of Electrical Engineering from 2003 to 2005, and with the Virtual Centre for Industrial Process Tomography from 2005 to 2009.

Prof. McCann was a fellow of the Royal Academy of Engineering in 2009.